Supplementary Material for: "Wavelength- and Structure-Insensitive On-Chip Mode Manipulation Based on the Thouless Pumping Mechanism"

Yingdi Pan,[a] Lu Sun,[a,*] Jingchi Li,[a] Qiyao Sun,[a] Pan Hu,[a] Songyue Liu,[a] Qi Lu,[a] Xiong Ni,[a] Xintao He,[b] Jianwen Dong,[b,*] and Yikai Su[a,*]

[a] State Key Lab of Advanced Optical Communication Systems and Networks, Department of Electronic Engineering, Shanghai Jiao Tong University, 200240, Shanghai, China
[b] State Key Laboratory of Optoelectronic Materials and Technologies, School of Physics, Sun Yat-Sen University, 510275, Guangzhou, China

This document provides the supplementary information for "Wavelength- and Structure-Insensitive On-Chip Mode Manipulation Based on the Thouless Pumping Mechanism". In Section 1, we present the theory of the Thouless pumping process in a Rice-Mele modeled waveguide array. Section 2 describes the methods used in the design, simulation, fabrication and characterization of the devices. Section 3 shows the simulation results of the mode-order conversions based on conventional asymmetric directional couplers (ADCs). In Section 4, we display the experimental results of the mode-division multiplexers based on ADCs. Section 5 shows the design of topological mode-order converters working for the TE polarization.

*****Lu Sun**,** E-mail: sunlu@sjtu.edu.cn
*Jianwen Dong, E-mail: dongjwen@mail.sysu.edu.cn
*****Yikai Su**,** E-mail: yikaisu@sjtu.edu.cn

1 Theory of the Thouless Pumping Process in a Rice-Mele Modeled Waveguide Array

Here, we use the tight binding model to describe the light propagation and coupling in the waveguide array in Figure 1(a) of the main text. The Hamiltonian which describes the dynamics of the mode evolution has the following form[29,30]:

$$H = \frac{1}{2}h(z)\sum_i (-1)^i c_i^\dagger c_i + \frac{1}{2}\sum_i [\tau + (-1)^i \delta(z)] c_i^\dagger c_{i+1} + h.c., \tag{S1}$$

where $h(z) = h_0 \sin 2\pi z$ is the mode mismatching modulation corresponding to the variation in on-site energy, and $\delta(z) = e^{\delta_0 \cos 2\pi z} - 1$ is the coupling strength modulation related to the variation in hopping strength between neighboring sites. $c_i^\dagger$ and c_i are the creator and annihilator on lattice site i, τ is the average coupling strength, and z is the normalized propagation distance. We consider an array with $2N$ waveguides with the odd- and even-numbered waveguides being the narrow and wide waveguides, respectively. Then the fundamental mode in the narrow waveguide and the high-order mode in the wide waveguide should

have equal effective indices. Substituting the Hamiltonian into the Schrodinger equation, we can derive the equations of the coupled mode theory (CMT) as follows[43]:

$$i\frac{d}{dz}\begin{pmatrix} A_1 \\ A_2 \\ \vdots \\ A_{2N-1} \\ A_{2N} \end{pmatrix} = \begin{pmatrix} h & \tau-\delta & & & & \\ \tau-\delta & -h & \tau+\delta & & & \\ & \tau+\delta & \ddots & \tau+\delta & & \\ & & \tau+\delta & h & \tau-\delta & \\ & & & \tau-\delta & -h & \end{pmatrix}_{2N\times 2N} \begin{pmatrix} A_1 \\ A_2 \\ \vdots \\ A_{2N-1} \\ A_{2N} \end{pmatrix}, \tag{S2}$$

where $i=\sqrt{-1}$ is the imaginary unit, and A_n stands for the field intensity in waveguide n. Note that it represents the field intensity of the fundamental mode for the odd number *n* and that of the high-order mode for the even number *n*. By solving the eigen mode problem for the $2N\times 2N$ tridiagonal matrix on the RHS of Equation S2, we can find a left edge mode $(1\ 0\ R\ 0\ R^2\ 0\ R^3\ 0\ ...)^{\mathrm{T}}/\sqrt{\Omega}$ and a right edge mode $(...\ 0\ R^3\ 0\ R^2\ 0\ R\ 0\ 1)^{\mathrm{T}}/\sqrt{\Omega}$ when $z\in[0,1/4)\bigcup(3/4,1]$. Ω is the normalization factor and $R=-(\tau-\delta)/(\tau+\delta)$ is the attenuation coefficient of the edge mode. We also know from the Bloch theorem that for the left edge mode the Bloch wave number k satifies $e^{ik}=-(\tau-\delta)/(\tau+\delta)$ and $e^{-ik}=-(\tau+\delta)/(\tau-\delta)$ [44], which leads to the following relation:

$$\cos k=\frac{e^{ik}+e^{-ik}}{2}=-\frac{\tau-\delta}{\tau+\delta}-\frac{\tau+\delta}{\tau-\delta}=-\frac{\tau^2+\delta^2}{\tau^2-\delta^2}. \tag{S3}$$

Similarly, for the right edge mode it becomes $e^{-ik}=-(\tau-\delta)/(\tau+\delta)$ and $e^{ik}=-(\tau+\delta)/(\tau-\delta)$, so Equation S3 is also valid for the right edge mode. We can rewrite Equation S1 in momentum space, which gives[45]:

$$H=\sum_k\left(a_k^{\dagger}\ b_k^{\dagger}\right)\mathbf{d}(k)\bullet\boldsymbol{\sigma}\begin{pmatrix} a_k \\ b_k \end{pmatrix}, \tag{S4}$$

where **d** = (d_x, d_y, d_z) is defined by $d_x=\frac{1}{2}(\tau+\delta)+\frac{1}{2}(\tau-\delta)\cos k, d_y=-\frac{1}{2}(\tau-\delta)\sin k, d_z=h$, and **σ** = ($\sigma_x$, σ_y, σ_z) by the Pauli matrices $\sigma_{x,y,z}$. The eigen values of the Hamiltonian or equivalently the effective indices of the modes can be expressed as:

$$n_{eff} = \sqrt{\frac{1}{2}(\tau^2 + \delta^2) + \frac{1}{2}(\tau^2 - \delta^2)\cos k + h^2}. \quad \text{(S5)}$$

We know that $n_{eff} = \pm h$ for $z \in [0,1/4) \bigcup (3/4,1]$, which leads to $\cos k = -\frac{\tau^2 + \delta^2}{\tau^2 - \delta^2}$. This is exactly the same expression in Equation S3, proving that we can draw the same conclusion in real space and momentum space.

It is worth mentioning that we can observe multiple band gaps and edge states in the band structure of the transverse magnetic (TM) supermodes in a Rice-Mele (RM) modeled waveguide array. As shown in Figure S1(a), apart from the pair of edge states that we focus on throughout the study (indicated by the red and blue solid lines) there are also two edge states appearing in the first and third band gaps of the band diagram (indicated by the green and purple solid lines). Figure S1(b) displays the electric field distribution (Re(E_y)) of the supermodes at Points I and II in Figure S1(a). They show clear characteristics of edge modes when located in the middle of the band gap. However, the mode evolution along the green and purple curves does not follow the Thouless pumping process and the underlying mechanism is yet to be revealed. Fortunately, these two states are positioned far away in effective modal index from the supermodes we discussed in the main text (represented by the red and blue solid lines in the band diagram) and therefore have little influence on the conclusions we have drawn about the pair of edge states appearing in the second band gap.

The adiabatic evolution of the supermodes along the red and blue curves in Figure S1(a) follows the Thouless pumping process. The modes are initially located in the band gap and spatially localized on one edge. Then they gradually approach the bulk bands and the modal fields become fully delocalized. Finally, the modes are located in the band gap again and the fields become highly localized on the opposite edge. The adiabatic evolution completes the edge-to-edge transport of light in one pump cycle. The deviations in structural parameters such as waveguide width and gap distance will cause some changes to the band structure in Figure S1(a). However, they will not change the process that the red and blue curves start from the middle of the band gap, get immersed into the bulk bands, and then return to the middle of the band

gap. This corresponds to the Thouless pumping process which gives rise to the robust transport of light from one edge of the waveguide array to the other. Therefore, this is a global topological property that is insensitive to some local deformations of the band structure during the mode evolution. That is the reason why our topological design shows significant robustness to the deviations in structural parameters. The feature can be reflected by an indicator which is also known as the topological invariant. Since the mode mismatching strength h and the mode coupling strength δ vary periodically along the propagation direction, they form a closed loop in the (h, δ)-space, as schematically illustrated in Figure S1(c). When the loop encloses the origin point, the Chern number equals 1 and the transport of light across the waveguide array is topologically protected. On the other hand, when the area encircled by the closed loop does not contain the origin point, the Chern number is 0 and the Thouless pumping process does not occur. The structural deviations will result in the deformations of the parametric loop. However, unless the perturbations are strong enough to change the loop from enclosing the origin point to not enclosing it, the transport of light is topologically protected and therefore the performance of the devices based on the Thouless pumping mechanism is well preserved.

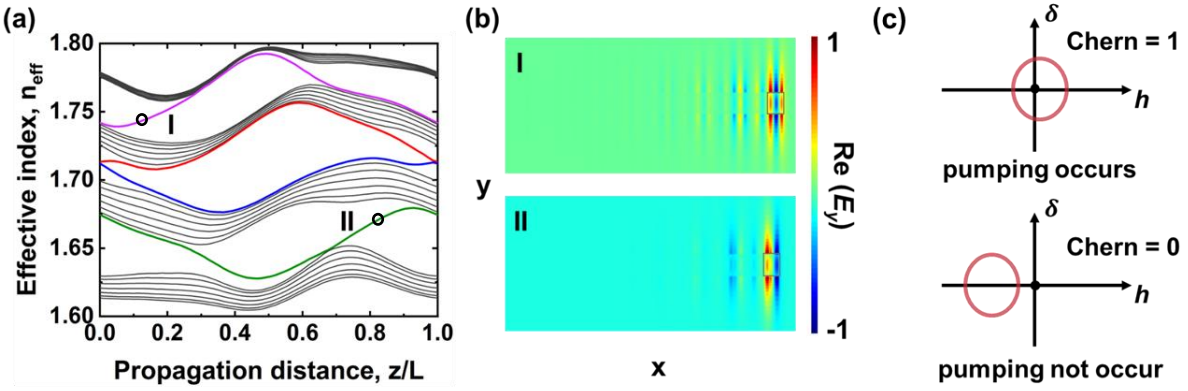

Figure S1. Evolution of the TM supermodes in a RM modeled silicon waveguide array. a, Band structure of the TM supermodes in an array of 30 waveguides with alternating waveguide widths over one pump cycle. The black solid lines represent the bulk bands while the green, blue, red and purple solid lines represent the edge modes when they locate in the middle of the band gap. **b,** Electric field distribution (Re(E_y)) of the supermodes at Points I and II in a. **c,** Schematics of the parametric loops in the (h, δ) -space when the structural parameters vary periodically along the propagation direction.

In the case of a waveguide array with just a few waveguides (e. g., a four-waveguide structure for topological mode manipulation in the main text), the edge-to-edge transport of the Thouless pump requires that the energy levels of the edge modes [red and blue curves in Figure S2(a)] start from the middle of the gap between two bulk energy levels [black curves in Figure S2(a)], approach the bulk energy levels during propagation and finally get back to the middle of the gap. This phenomenon depends on whether or not the parametric loop in the (h, δ)-space encircles the origin point, as illustrated in Figure S2(b). An indicator can be defined to reflect the loop encircling the origin point or not. In the case of a waveguide array with a large number of waveguides, the indicator happens to be the Chern number as it equals to 1 for encircling the origin [Figure S1(c)] and 0 for not encircling the origin [Figure S1(d)]. For an array with only a few waveguides, the indicator can be directly defined to be 1 (0) for (not) encircling the origin without calculating the Chern number. Since this is a global property that does not change with some continuous deformations of the parametric loop, the topological protection still exists in the system with only a few waveguides and the indicator defined above can be considered as a topological invariant.

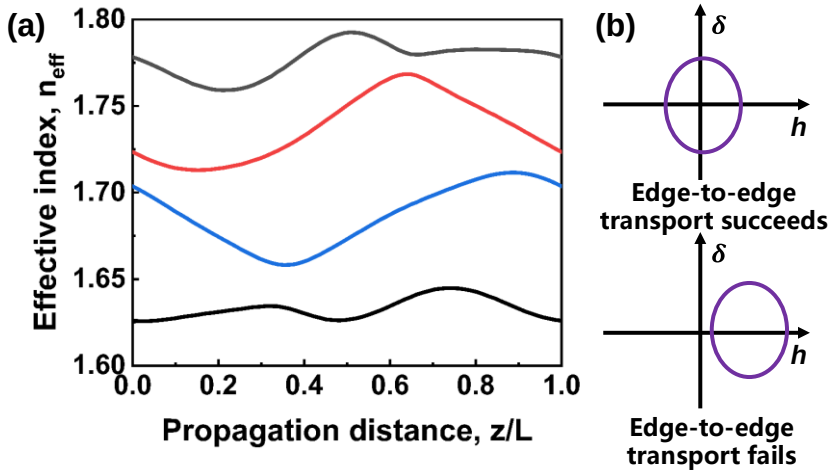

Figure S2. Thouless pumping process in a four-waveguide array. a, Band structure of the TM supermodes in an array of 4 waveguides with alternating waveguide widths over one pump cycle. The black solid lines represent the bulk energy levels while the red and blue solid lines represent the edge modes when they locate in the middle of the gap between two bulk energy levels. **b,** Schematics of the parametric loops in the (h, δ)-space in a four-waveguide array when the structural parameters vary periodically along the propagation direction.

2 Device Design, Simulation, Fabrication and Characterization

We design the silicon waveguide array to implement the RM model whose Hamiltonian is given by Equation S1. As shown in Figure 2(b) of the main text, the waveguide widths are varied along the propagation direction to realize the mode mismatching strength $h(z)$. The silicon waveguides are 220 nm in height and surrounded by silica cladding. The refractive indices of silicon and silica are $n_{\mathrm{Si}} = 3.455$ and $n_{\mathrm{SiO_2}} = 1.445$ respectively at a central wavelength of 1550 nm. The effective indices of the TM_0-TM_3 modes in a single waveguide can be calculated using the commercial eigenmode solver (Lumerical MODE Solutions) as functions of waveguide width, which are shown in Figure S3(a). The relationship between the effective modal index n_{eff} and the waveguide width can be approximated by the following quadratic polynomial:

$$n_{eff} = A\Delta w^2 + B\Delta w + C, \tag{S6}$$

where *A*, *B* and *C* are the fitting constants, and Δw is the waveguide width variation with respect to the average value $\overline{w}$ (see Table 1 in the main text). The coupling strength κ between two modes can be controlled by the waveguide separation and calculated using the even- and odd-mode analysis[46]:

$$\kappa = k_0 (n_{even} - n_{odd}) / 2, \tag{S7}$$

where k_0 is the wave number of light in vacuum at 1550 nm, and n_{even} and n_{odd} are the effective indices of the even and odd supermodes. As shown in Figure S3(b), the relation between the coupling strength and the gap width can be described by:

$$\kappa = \kappa_0 \exp(-\alpha g), \tag{S8}$$

where *g* is the spacing between waveguides, and κ_0 and α are the magnitude and the decay coefficient, respectively. We choose proper waveguide width and gap width so that the modal effective indices of the TM_0-TM_3 modes vary in the range of 1.69-1.72 and the coupling strengths between the TM_0 mode and the TM_1-TM_3 modes change in the ranges of $0.017\,k_0$-$0.075\,k_0$, $0.011\,k_0$-$0.052\,k_0$ and $0.008\,k_0$-$0.041\,k_0$,

respectively. The periodicity L along the propagation direction is designed to be much longer (over 10 times) than the coupling length L_c for the average coupling strength τ which can be calculated by $L_c = \pi / 2\tau$. In our design, we choose L = 80 μm, 150 μm and 200 μm for the TM_0-to-$TM_{1,2,3}$ conversions, respectively.

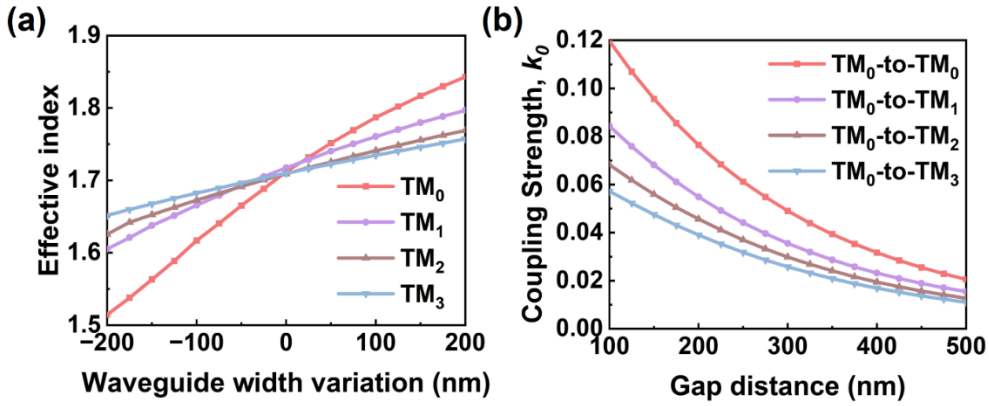

Figure S3. Details on the device design. a, Effective indices of the TM_0-TM_3 modes as functions of waveguide width variation Δw with respect to the average value $\overline{w}$. **b,** Coupling strengths in units of k_0 between the TM_0 mode and the TM_0-TM_3 modes as functions of gap distance between two neighboring waveguides.

Full-wave numerical simulations were carried out using three-dimensional finite-difference time-domain (3D FDTD) methods (Lumerical FDTD Solutions). The dispersion relationships of the refractive indices of silicon and silica were taken from Palik's handbook of optical constants[47]. The mode expansion monitor was used to calculate the mode overlapping constants between the optical fields at the output ports of the devices and those of the waveguide eigenmodes. Consequently, we can selectively derive the transmission of any mode to characterize the insertion loss (IL) and intermodal crosstalk (CT) of the proposed devices.

The topological devices and their conventional counterparts were fabricated on a silicon-on-insulator (SOI) wafer (220-nm-thick top silicon layer and 3-μm-thick buried oxide layer). The fabrication process is schematically illustrated in Figure S4. The wafer was first cleaned in ultrasound baths of acetone and isopropyl alcohol (IPA) for 5 minutes and then rinsed in deionized (DI) water for 1 minute. After drying up with nitrogen flow, it was further cleaned by O_2 plasma asher. Then the AR-P 6200.09 photoresist was spin-coated onto the chip and prebaked at 150 °C for 1 minute. E-beam lithography (EBL, Vistec RBPG 5200$^+$)

was used to define the patterns of the grating couplers (GCs). The photoresist was developed in methyl isobutyl ketone (MIBK) for 75 seconds and then rinsed in IPA for 1 minute. After that, the chip was dried with nitrogen flow and the patterns were transferred onto the top silicon layer using inductively coupled plasma (ICP, SPTS DRIE-I) dry etching with an etching depth of 70 nm. The remaining photoresist was removed using acetone, IPA and DI water. Then the procedure described above was repeated to fabricate the other structures including the waveguide arrays and the mode (de)multiplexers, but this time with an etching depth of 220 nm. Finally, a 1-μm-thick silica cladding layer was deposited onto the chip by plasma enhanced chemical vapor deposition (PECVD, Oxford Plasmalab System 100). The fabricated samples were inspected using the optical microscope and the scanning electron microscope (SEM, Zeiss Ultra Plus).

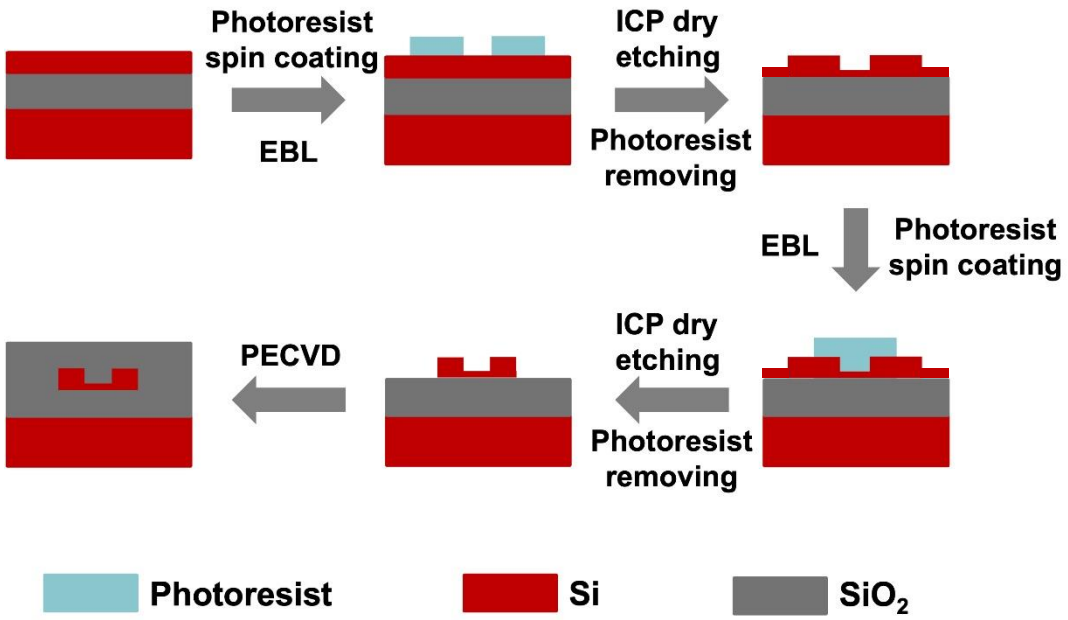

Figure S4. Schematic of the device fabrication process. EBL and ICP etching were applied twice to form the waveguides and the GCs. PECVD was employed to deposit the silica upper cladding layer over the devices.

The experimental setup for the transmission measurement of the devices is shown in Figure S5. A tunable continuous wave (CW) laser (Santec TSL-770) and a photodetector (PD, Santec MPM-210) were employed to measure the transmission spectra of the devices. The polarization of light was adjusted by a fiber polarization controller (PC) before the TM-polarized light was coupled into and out of the chip by

GCs. The fiber-chip coupling loss was ~6 dB/facet at the central wavelength of 1550 nm. The output light was split into two paths through a 3-dB fiber coupler. One half was guided into a power meter (PM) for optical calibration while the other half was directed into a PD to measure the transmitted power. The tunable laser and the PD were controlled by a computer to record the optical power at every wavelength in the range of 1500-1600 nm. The transmission spectra of the devices were all normalized to that of the reference GCs fabricated on the same chip.

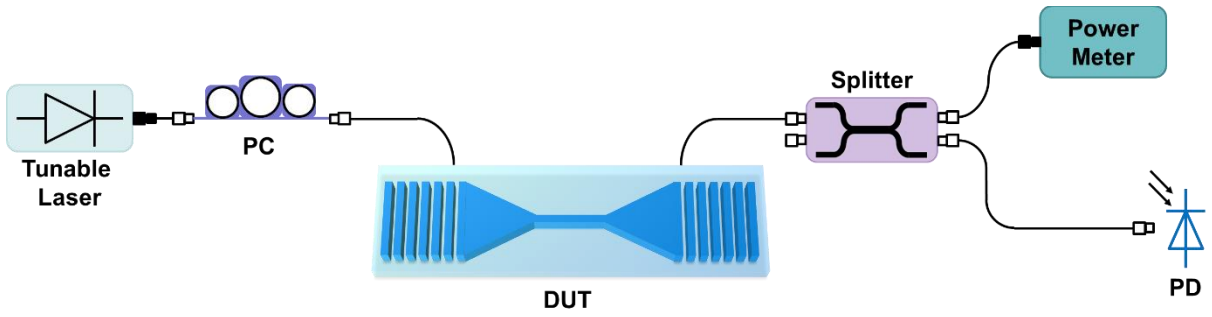

Figure S5. Schematic of the experimental setup for the transmission measurement. DUT: device under test, PC: polarization controller, PD: photodetector.

The experimental setup and the DSP flow charts for the 50-GBaud 16-QAM signals transmission experiment are shown in Figure 7(a),(b) in the main text. At the transmitter, a QAM data stream was up-sampled and then processed by a root-raised cosine (RRC) filter with a rool-off factor of 0.01. After resampling, the QAM signal was sent to a 100 GSa/s digital-to-analog converter (DAC, Micram DAC4). The output signal of the DAC was amplified by the electrical amplifier (EA) to drive a 35-GHz in-phase and quadrature modulator (IQM) biased at its transmission null. A 10-dBm continuous light from an external cavity laser (ECL) was amplified by an erbium-doped fiber amplifier (EDFA) and then injected into the IQM. The generated optical signal was boosted by the second EDFA and then coupled into and out of the device. The receiver consists of an EDFA to compensate for the optical loss, a coherent receiver to detect the signal, and a 160 GSa/s digital storage oscilloscope (DSO) (LeCroy 36Zi-A) to recover the data. In the receiver DSP, the signal was first resampled and then processed by the frequency offset compensation (FOC), root-raised cosine (RRC) filtering and synchronization. Then, a 2 × 2 multiple-input and multiple-

output-feedforward equalizer (MIMO-FFE) was used for channel equalization. Besides, a post-filter (PF) and a maximum-likelihood sequence decision (MLSD) were implemented to mitigate the influence of the noise enhancement effect of the FFE. Finally, the BER of the system was calculated and analyzed.

3 Mode-Order Conversions Based on Conventional Asymmetric Directional Couplers

To compare with the mode-order conversions realized in topological waveguide arrays, we design three mode-order converters based on asymmetric directional couplers (ADCs) for the TM_0-to-TM_1, TM_0-to-TM_2 and TM_0-to-TM_3 conversions. We use the 3D FDTD methods to simulate the ADC structures and find out the IL and CT of each mode. The simulated transmission spectra of the three converters are displayed in Figure S6. The ILs are less than 2 dB at 1550 nm but they drop very quickly when deviating from the central wavelength. The 3-dB bandwidths of the target modes are only 40 nm, 37 nm and 25 nm for the TM_0-to-TM_1, TM_0-to-TM_2 and TM_0-to-TM_3 mode-order converters, respectively. The CT values are lower than -10 dB in the wavelength range of 1500-1600 nm. Comparing with the simulated transmission spectra of the topological design in Figure 2 (e)-(g) of the main text, we are convinced that the mode-order conversions based on the Thouless pumping mechanism are more tolerant to the wavelength variation.

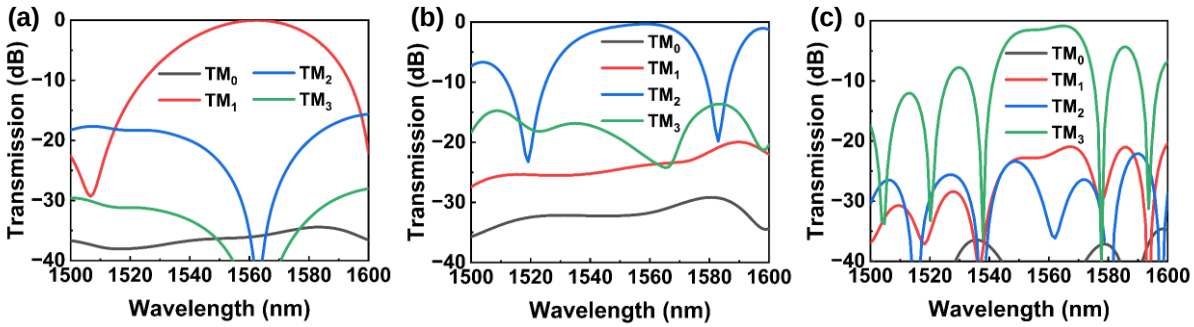

Figure S6. Simulated transmission spectra of the **a,** TM_0-to-TM_1, **b,** TM_0-to-TM_2 and **c,** TM_0-to-TM_3 mode-order converters based on ADCs.

4 Mode-Division Multiplexer Based on Conventional Asymmetric Directional Couplers

The conventional mode-order converters based on ADCs were cascaded to form the four-channel mode-division multiplexer, as shown in Figure 4 of the main text. The measured transmission spectra are plotted in Figure S7(a)-(d) when the light is injected from the TM_0-TM_3 ports on the left side of the device, respectively. Obviously, the 3-dB bandwidth of the conventional device is much narrower than that of the topological design (cf. Figure 5 in the main text), especially that the 3-dB bandwidth of the TM_3 mode channel is only ~10 nm. Also, the central wavelengths of the mode channels are inevitably blue-shifted due to the fabrication errors. These results clearly reveal that the topological mode multiplexer outperforms its conventional counterpart based on ADCs in working bandwidth and fabrication tolerance.

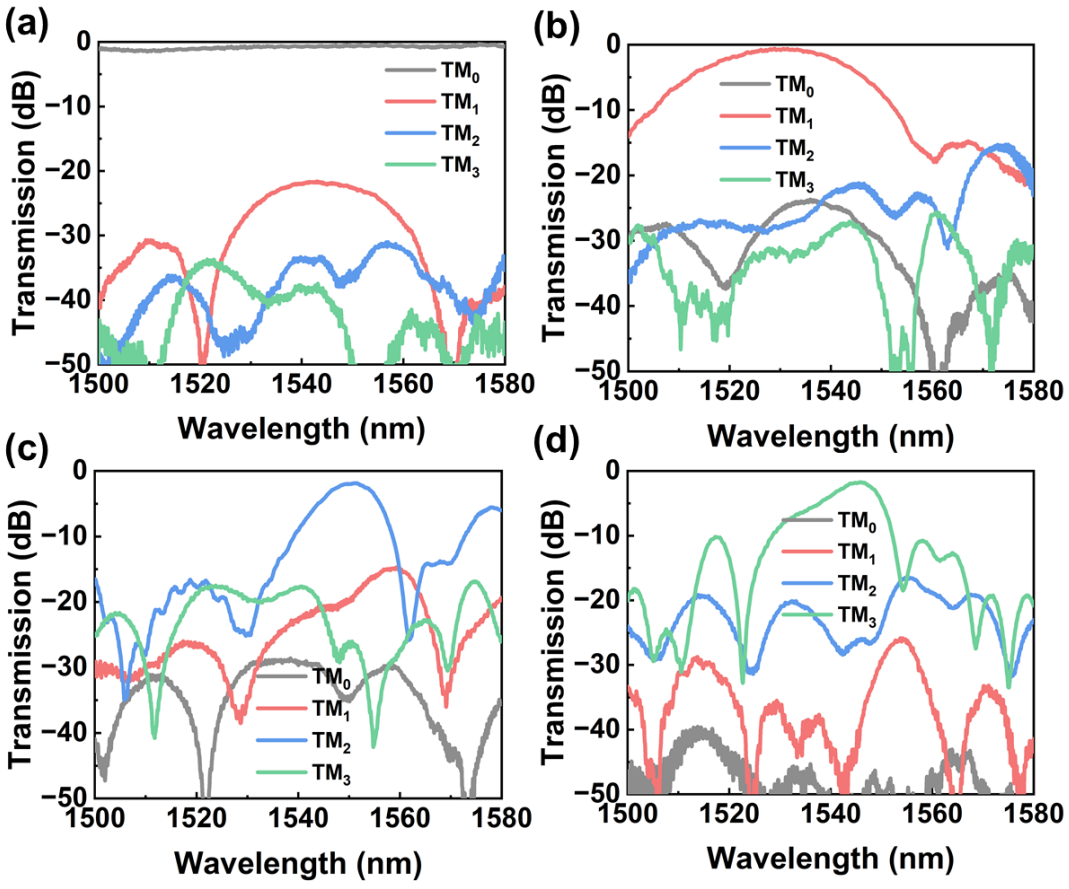

Figure S7. Measured transmission spectra of the conventional mode-division multiplexer based on ADCs when the light is injected from the **a,** TM_0, **b,** TM_1, **c,** TM_2 and **d,** TM_3 input ports on the left side of the device.

5 Topological Mode-Order Converters Working for TE Polarization

The topological design method based on the Thouless pumping mechanism can also be applied to the mode manipulation for the transverse electric (TE) polarization. Here, we show the design details of the TE_0-to-TE_1, TE_0-to-TE_2 and TE_0-to-TE_3 mode-order converters. The designed values of the structural parameters of the topological waveguide arrays are listed in Table S1.

Table S1. Design parameters for different TE mode-order conversions

Mode-Order Conversion	$\overline{w_1}$ (nm)	Δw_1 (nm)	$\overline{w_2}$ (nm)	Δw_2 (nm)	$\overline{g}$ (nm)	Δg (nm)	L (μm)
TE_0-to-TE_1	360	[-15,15]	760	[-22,22]	210	[-140,140]	150
TE_0-to-TE_2	360	[-20,20]	1160	[-35,35]	200	[-135,135]	200
TE_0-to-TE_3	360	[-12,12]	1560	[-21,21]	235	[-135,135]	260

We use the 3D FDTD methods to conduct the full-wave simulations of the mode-order conversions in the topological waveguide arrays. Figure S8(a)-(c) presents the simulated light propagation profiles ($|E_x|$) at 1550 nm in the TE_0-to-TE_1, TE_0-to-TE_2 and TE_0-to-TE_3 mode conversion regions with the corresponding transmission spectra of the three mode-order converters displayed in Figure S8(d)-(f). The ILs are lower than 0.98 dB, 1.07 dB and 0.92 dB over a 100-nm bandwidth (1500-1600 nm) for the TE_1, TE_2 and TE_3 mode conversions, respectively. The CT values are below -20.5 dB, -22.4 dB and -36.5 dB in the same wavelength range for the three mode-order converters. The device has similar performance to that for the TM polarization, but with a larger footprint and a smaller feature size due to the weaker coupling strengths between the TE modes. Future works based on the TE-polarized topological design could be envisioned, for example, four-channel TE mode multiplexers or eight-channel mode- and polarization-division

hybrid multiplexers, which would drastically increase the link capacity of the on-chip optical interconnection system.

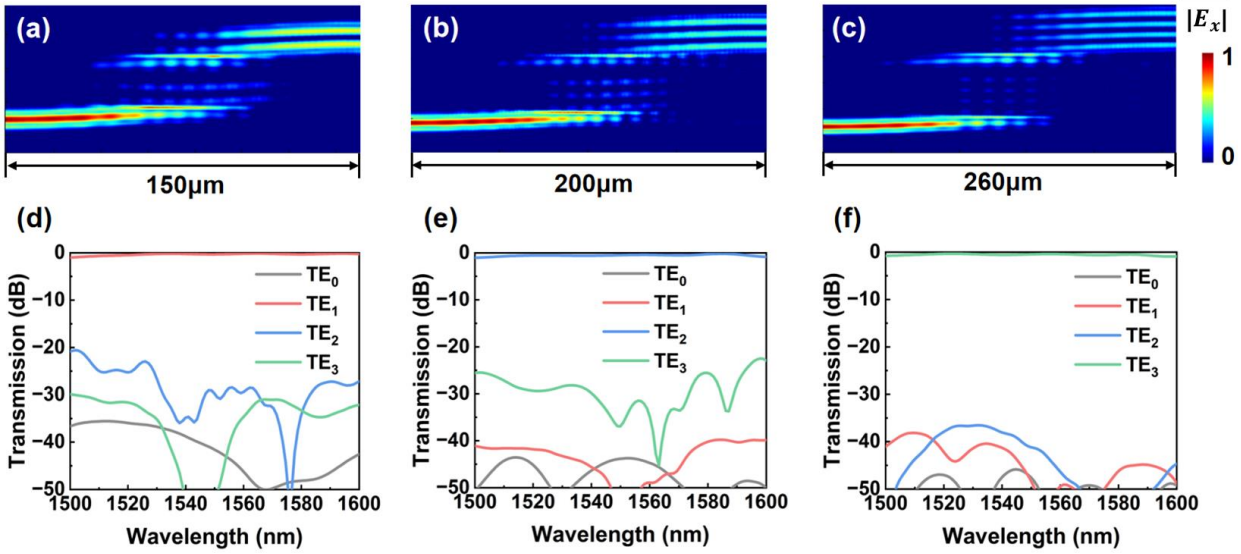

Figure S8. Topological mode-order converters working for the TE polarization. **a-c,** Light propagation profiles ($|E_x|$) in the **a,** TE_0-to-TE_1, **b,** TE_0-to-TE_2 and **c,** TE_0-to-TE_3 coupling regions. d-f) Simulated transmission spectra of the **d,** TE_0-to-TE_1, **e,** TE_0-to-TE_2 and **f,** TE_0-to-TE_3 mode-order converters.